

Photophysical and Photocatalytic Activities of a Novel Photocatalyst $\text{BaZn}_{1/3}\text{Nb}_{2/3}\text{O}_3$

Jiang Yin,[†] Zhigang Zou,[‡] and Jinhua Ye^{*,†,§}

PRESTO, Japan Science and Technology Agency, 4-1-8 Honchou Kawaguchi, Saitama, Japan,
Ecomaterials and Renewable Energy Research Center (ERERC), Nanjing University, 22 Hankou Road,
Nanjing 210093, China, and Ecomaterials Center, National Institute for Materials Science (NIMS),
1-2-1 Sengen, Tsukuba, Ibaraki 305-0047, Japan

Received: April 9, 2004; In Final Form: June 24, 2004

A new ABO_3 perovskite photocatalyst $\text{BaZn}_{1/3}\text{Nb}_{2/3}\text{O}_3$ has been synthesized by a solid-state reaction process. Nine Raman active vibration modes observed from its Raman scattering spectrum suggest that $\text{BaZn}_{1/3}\text{Nb}_{2/3}\text{O}_3$ possesses a distorted perovskite structure. The formation rate of H_2 evolution from $\text{CH}_3\text{OH}/\text{H}_2\text{O}$ solution with 5.0 wt % Pt cocatalyst under the irradiation of a 400 W Hg lamp is about $2685.7 \mu\text{mol}/(\text{h} \cdot \text{g catal})$ for the photocatalyst $\text{BaZn}_{1/3}\text{Nb}_{2/3}\text{O}_3$. It also splits pure water into H_2 and O_2 in a stoichiometric ratio with NiO_x and RuO_2 cocatalysts under UV light irradiation. The formation rates of the H_2 and O_2 evolution from pure water in the case of 1.0 wt % NiO_x cocatalyst under UV light irradiation are 291.22 and $145.61 \mu\text{mol}/(\text{h} \cdot \text{g catal})$, respectively. The photoelectrochemical properties of $\text{BaZn}_{1/3}\text{Nb}_{2/3}\text{O}_3$ film as deposited by using a pulsed laser deposition (PLD) technique suggested that the lower conduction band should be composed of the Zn^{2+} 4s state, which is in good agreement with its UV–vis diffuse reflectance spectrum.

I. Introduction

Water-splitting into H_2 and O_2 with semiconductor photocatalysts under photon irradiation has attracted much attention due to its prospects in conversion of solar energy and preservation of the environment.^{1–3} It has been reported that TiO_2 ,⁴ Ta_2O_5 ,⁵ $\text{Sr}_2\text{Ta}_2\text{O}_7$,⁶ $\text{K}_4\text{Nb}_6\text{O}_{17}$,⁷ La:NbTaO_3 ,⁸ and $\text{Ln}_2\text{Ti}_2\text{O}_7$ (Ln: rare earth),⁹ etc. show favorable photocatalytic activity under UV light irradiation, although the relationship between the crystal and electronic structures and their photocatalytic activities has not been well established. To develop a photocatalyst with high photocatalytic activity, great efforts have recently been made to understand what kind of the mechanism dominates the photocatalytic activity of the semiconductors.^{10–12} It is known that the tetrahedrally coordinated semiconductors ZnS and CdS show favorable photocatalytic activity under UV or visible light irradiation,^{13,14} although they are unstable chemically. Their excellent photocatalytic activities are ascribed to their special band structure, where the empty ns^0 orbitals and the fully occupied $(n-1)d^{10}$ orbitals construct their band structures. In previous works, we have developed several visible-light driven photocatalysts with ABO_3 perovskite structure in a charge-balanced manner by controlling the crystal and electronic structures, such as $\text{BaIn}_{1/2}\text{Nb}_{1/2}\text{O}_3$ and $\text{BaCo}_{1/3}\text{Nb}_{2/3}\text{O}_3$, etc.^{15,16} For developing Zn-containing ABO_3 photocatalysts with good photocatalytic activity, we report in this work a new perovskite photocatalyst, $\text{BaZn}_{1/3}\text{Nb}_{2/3}\text{O}_3$, which split water into H_2 and O_2 under UV light irradiation.

II. Experimental Section

The photocatalyst $\text{BaZn}_{1/3}\text{Nb}_{2/3}\text{O}_3$ was prepared by a solid-state reaction process with pure starting materials including BaCO_3 , ZnO and Nb_2O_5 . The well-mixed powders in stoichio-

metric ratio were preheated at 900 °C for 8 h. The reground powder was then sintered at 1200 °C for 32 h. The crystal structure of the photocatalyst powder was determined by using X-ray diffraction (JEOL JDX-3500), and the morphology of the $\text{BaZn}_{1/3}\text{Nb}_{2/3}\text{O}_3$ powder was observed by using a scanning electron microscope (JEOL JSM-6500). The surface area of the photocatalyst particles was measured by using the BET method (Shimadzu Gemini Micromeritics). The UV–vis diffuse reflectance spectrum of the sample was measured by using a UV–vis spectrometer (Shimadzu UV-2500PC). Raman scattering spectrum measurements were performed by using a laser Raman spectrophotometer (Jasco NRS-1000) at room temperature. The power of the incident laser beam was 100 mW with monochromatic wavelength 532 nm. The exposure time was 2 s.

The photocatalytic reactions were performed with a closed gas circulation system. An inner-irradiation type quartz cell with a 400 W high-pressure Hg lamp was employed. The gas evolved was determined with a TCD gas chromatograph (Shimadzu GC-8A), which was connected to the system with a circulating line. The Pt cocatalysts were loaded on the surface of the photocatalyst particles in the photocatalytic reactions performed in $\text{CH}_3\text{OH}/\text{H}_2\text{O}$ solution in order to obtain high activity.¹⁷ For splitting pure water, the NiO_x and RuO_2 cocatalysts were loaded on the photocatalyst powder from aqueous $\text{Ni}(\text{NO}_3)_2$ and RuCl_3 solutions. The Ni-loaded photocatalysts were calcined at 500 °C for 1 h and then reduced at 500 °C for 2 h in a mixed atmosphere of Ar and H_2 ($\text{Ar}:\text{H}_2 = 9:1$ in volume). Finally, the H_2 -treated photocatalysts were calcined at 200 °C for 1 h in pure O_2 atmosphere in order to get the NiO_x/Ni bilayer structure on the surface of the photocatalyst particles, which is known as the optimum condition for the Ni-loaded perovskite oxides.¹⁸ The Ru-loaded photocatalyst was only calcined at 500 °C for 1 h.

The photoelectrochemical properties of $\text{BaZn}_{1/3}\text{Nb}_{2/3}\text{O}_3$ were investigated with the heterostructure $\text{BaZn}_{1/3}\text{Nb}_{2/3}\text{O}_3/\text{ITO}/\text{quartz}$, where ITO (tin doped In_2O_3) acts as a conductive bottom electrode. The heterostructure $\text{BaZn}_{1/3}\text{Nb}_{2/3}\text{O}_3/\text{ITO}/\text{quartz}$ was

* Corresponding author. E-mail: jinhua.ye@nims.go.jp.

† PRESTO, Japan Science and Technology Agency.

‡ Nanjing University.

§ National Institute for Materials Science (NIMS).

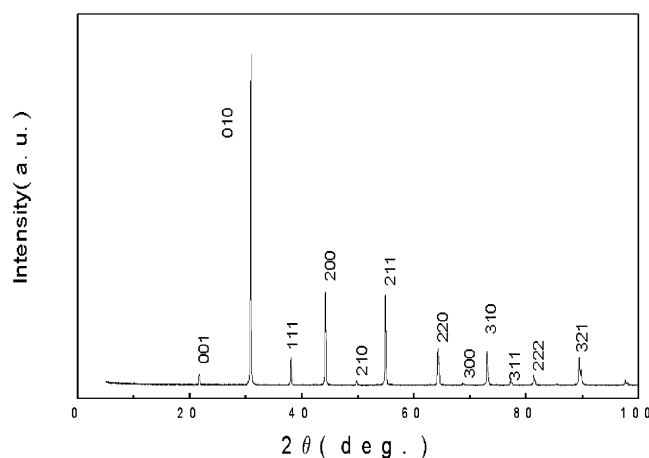


Figure 1. X-ray diffraction pattern of $\text{BaZn}_{1/3}\text{Nb}_{2/3}\text{O}_3$ powder.

deposited by using a pulsed laser deposition (PLD) technique at 850 °C. A pulsed laser Nd:YAG with an output wavelength 355 nm was employed, and the repetition rate was 10 Hz. The composition of the ITO target is 10 wt % SnO_2 -doped In_2O_3 . The O_2 (99.99995%) partial pressure of the chamber was 2.4×10^{-1} Torr during the deposition. The deposition time for $\text{BaZn}_{1/3}\text{Nb}_{2/3}\text{O}_3$ and ITO is 30 min. After the deposition, the heterostructure $\text{BaZn}_{1/3}\text{Nb}_{2/3}\text{O}_3/\text{ITO}/\text{quartz}$ was annealed in a quartz tube with flowing O_2 atmosphere at 850 °C for 2 h. After observing the cross section of the interface for the heterostructure $\text{BaZn}_{1/3}\text{Nb}_{2/3}\text{O}_3/\text{ITO}/\text{quartz}$ by using SEM, the thickness of the film ITO and $\text{BaZn}_{1/3}\text{Nb}_{2/3}\text{O}_3$ was estimated as about 10 μm .

Photoelectrolysis of water was performed in a Pyrex cell, which consisted of the photoanode, a Pt foil counter-electrode, a quartz window, and a saturated calomel electrode (SCE). The electrolyte is 0.1 M Na_2SO_4 solution (pH = 5.92). A Xe lamp (500 W, Ushio Denki Co.) was employed as the light source. Before the experiments, the electrolyte solution was flushed with N_2 to remove dissolved O_2 . The backside and the edge of the heterostructure BZNO/ITO/quartz was covered with insulating epoxy resin.

III. Results and Discussion

Structure Characterization. It was reported that $\text{BaZn}_{1/3}\text{Nb}_{2/3}\text{O}_3$ has a cubic ABO_3 perovskite structure with space group $Pm\bar{3}m$,¹⁹ in which the B site is occupied by two kinds of the transition metals randomly, similar to $\text{BaIn}_{1/2}\text{Nb}_{1/2}\text{O}_3$ and $\text{BaCo}_{1/3}\text{Nb}_{2/3}\text{O}_3$, as reported in our previous works.^{15,16} Figure 1 shows the X-ray diffraction pattern of $\text{BaZn}_{1/3}\text{Nb}_{2/3}\text{O}_3$ powder. The sample was well crystallized, and all of the diffraction peaks can be indexed. The surface area of the $\text{BaZn}_{1/3}\text{Nb}_{2/3}\text{O}_3$ powder is 1.24 m^2/g . Figure 2 shows the SEM morphology of $\text{BaZn}_{1/3}\text{Nb}_{2/3}\text{O}_3$ photocatalyst powder. The $\text{BaZn}_{1/3}\text{Nb}_{2/3}\text{O}_3$ particles distribute dispersively, and the average particle size of the photocatalyst $\text{BaZn}_{1/3}\text{Nb}_{2/3}\text{O}_3$ is about 150 nm.

Raman Scattering Spectrum. The Raman scattering spectrum and the IR reflection spectrum of ABO_3 perovskites have been widely investigated, both theoretically and experimentally.^{20–22} For the cubic perovskite, the normal modes of the lattice vibration at the zone center ($k = 0$, Γ) are given in the irreducible representation by

$$\Gamma^{\text{total}} = 4F_{1u} + F_{2u} \quad (1)$$

One of the F_{1u} modes corresponds to the acoustic phonon and F_{2u} is optically silent, i.e., neither IR nor Raman active, as shown

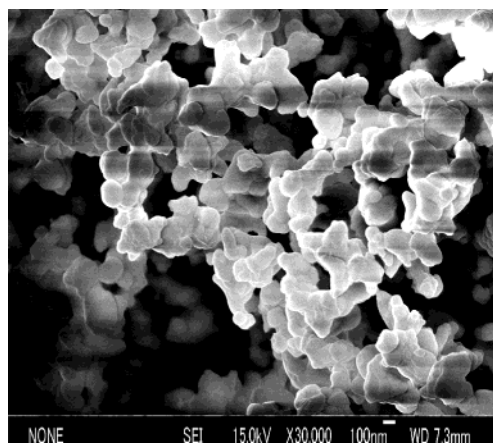


Figure 2. SEM morphology of $\text{BaZn}_{1/3}\text{Nb}_{2/3}\text{O}_3$ photocatalyst powder.

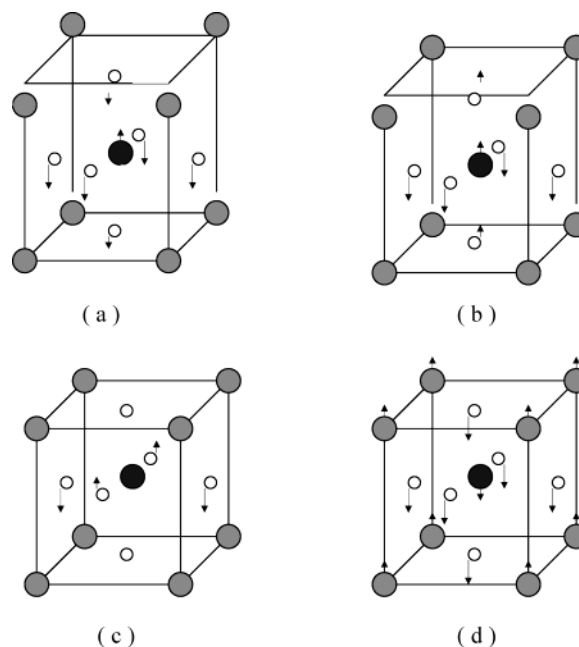


Figure 3. Optical phonon modes of the cubic perovskite ABO_3 : (a) stretching; (b) bending; (c) inactive; (d) external.

in Figure 3c. The remaining three F_{1u} modes are IR active, corresponding to three vibrational motions: (i) the B–O bond distance is modulated (the stretching mode); (ii) the B–O bond angle is modulated (the bending mode); (iii) atom A translates with respect to BO_6 octahedron (the external mode), as schematically drawn in Figure 3, parts a, b, and d, respectively. With the decrease of the crystal symmetry, the number of phonon modes increases in the distorted perovskite structure owing to the following two mechanisms: (1) the lowered symmetry lifts the 3-fold degenerate F_{1u} (F_{2u}) modes of the cubic structure; (2) the distortion enlarges the unit cell which contains more than two formula units, and as a result, the phonon branches are folded into the reduced Brillouin zone, resulting in an increase in the Γ -point phonon modes. Some of the modes are Raman active and some of them are IR active, or both are Raman and IR active.

Figure 4 shows Raman scattering spectrum of the photocatalyst $\text{BaZn}_{1/3}\text{Nb}_{2/3}\text{O}_3$ at room temperature. Nine modes around 94.25, 136.87, 160.72, 259.16, 282.56, 368.92, 421.17, 525.62, and 784.38 cm^{-1} can be observed clearly. Although the complete assignment is not possible because a polarization analysis is not available, according to the method adopted by Perry et al.²³ in the IR study of perovskite, from low to high-frequency we

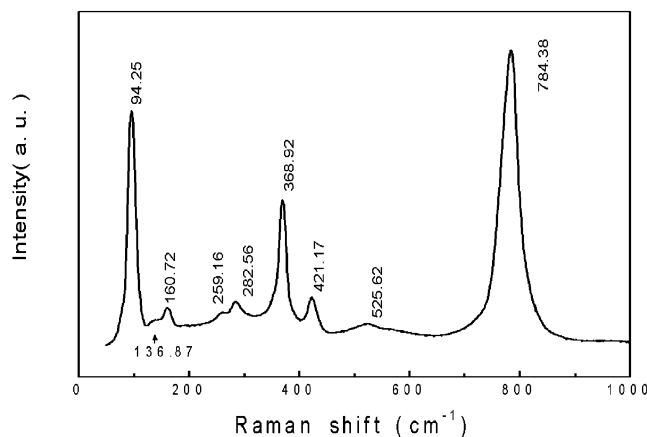


Figure 4. Raman scattering spectrum of the photocatalyst $\text{BaZn}_{1/3}\text{Nb}_{2/3}\text{O}_3$.

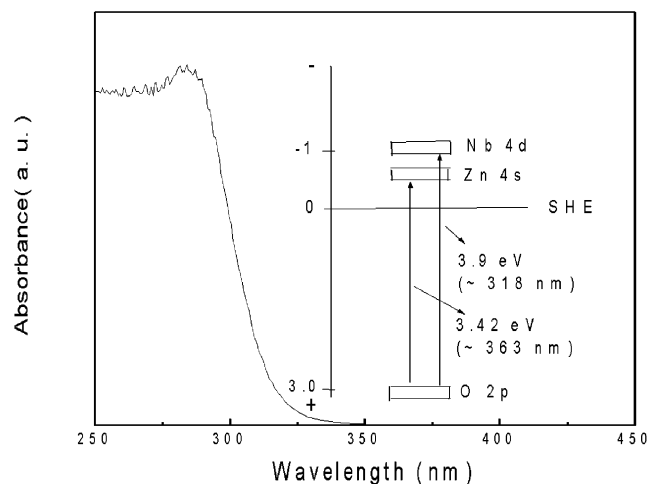


Figure 5. UV-vis diffuse reflectance spectrum of the photocatalyst $\text{BaZn}_{1/3}\text{Nb}_{2/3}\text{O}_3$.

can interpret the Raman spectrum of $\text{BaZn}_{1/3}\text{Nb}_{2/3}\text{O}_3$ as composed of three main phonon branches. The first mode at 94.25 cm^{-1} should be ascribed to the external mode, and the seven modes around 368.92 cm^{-1} should be ascribed to the bending branch. The last mode at 784.38 cm^{-1} should be ascribed to the stretching mode. The observed Raman active modes for $\text{BaZn}_{1/3}\text{Nb}_{2/3}\text{O}_3$ indicate that the distorted perovskite structure should be more reasonable for $\text{BaZn}_{1/3}\text{Nb}_{2/3}\text{O}_3$, just like for

$\text{BaIn}_{1/2}\text{Nb}_{1/2}\text{O}_3$.²⁴ The distortion of the octahedrons (ZnO_6 and NbO_6) in $\text{BaZn}_{1/3}\text{Nb}_{2/3}\text{O}_3$ may be very small, and the structural deviation is not large enough to be detected by X-ray diffraction. So from the X-ray diffraction pattern, $\text{BaZn}_{1/3}\text{Nb}_{2/3}\text{O}_3$ still shows a cubic ABO_3 perovskite structure.

Photophysical Characterization. Figure 5 shows the UV-vis diffuse reflectance spectrum of the photocatalyst $\text{BaZn}_{1/3}\text{Nb}_{2/3}\text{O}_3$. The property of the optical transition in $\text{BaZn}_{1/3}\text{Nb}_{2/3}\text{O}_3$ was determined from Figure 5, as in our previous work.²⁵ It was found that, corresponding to the main UV light absorption, $\text{BaZn}_{1/3}\text{Nb}_{2/3}\text{O}_3$ is a direct semiconductor, and the optical transition is directly forbidden. The band gap as determined is 3.9 eV. The theoretical calculations on the electronic structures of the tetrahedrally coordinated ZnO , ZnS , and CdS ^{26,27} show that the conduction band of these compounds is mainly composed of the $\text{Zn}^{2+} 4s$ or $\text{Cd}^{2+} 5s$ state, so it is suggested that the conduction band of the octahedrally coordinated $\text{BaZn}_{1/3}\text{Nb}_{2/3}\text{O}_3$ should be mainly composed of the $\text{Zn}^{2+} 4s$ state and the $\text{Nb}^{5+} 4d$ state, and the valence band should be composed of the O 2p state. It is also obvious from Figure 5 that there exists a long tail for the spectrum in the long wavelength region, which may be ascribed to the electronic excitation from the O 2p state to the $\text{Zn}^{2+} 4s$ state.

Photocatalytic Reactions. For evaluating the photocatalytic activity of the photocatalyst $\text{BaZn}_{1/3}\text{Nb}_{2/3}\text{O}_3$, the easily oxidable reagent CH_3OH was employed. Figure 6a shows the formation rate of H_2 evolution from $\text{CH}_3\text{OH}/\text{H}_2\text{O}$ solution with different Pt-loadings under UV light irradiation for the photocatalyst $\text{BaZn}_{1/3}\text{Nb}_{2/3}\text{O}_3$ (catalyst, 0.5 g; CH_3OH , 50 mL; H_2O , 320 mL; 400 W Hg lamp). For a Pt-loading of 0.05 wt %, the H_2 formation rate is only $251.6\text{ }\mu\text{mol}/(\text{h}\cdot\text{g catal})$, while for a Pt-loading concentration of 5.0 wt %, the H_2 formation rate is $2658.7\text{ }\mu\text{mol}/(\text{h}\cdot\text{g catal})$, and in less than 4 h the pressure inside the cell reaches 1 atm. The relationship between the Pt-loading concentration and the H_2 formation rate is plotted in Figure 6b. When the Pt-loading is lower than 1.0 wt %, the H_2 formation rate increases quickly with increase in the Pt-loading. This should be ascribed to the increase of the active sites on the surface of the photocatalyst $\text{BaZn}_{1/3}\text{Nb}_{2/3}\text{O}_3$ due to the increase of the Pt concentration. After the Pt-loading is greater than 1.0 wt %, the slope of the curve decreases greatly although the H_2 formation rate still increases with the increase of the Pt-loading. It means that when the concentration of the Pt cocatalyst is over than 1.0 wt %, the photocatalytic activity of the photocatalyst

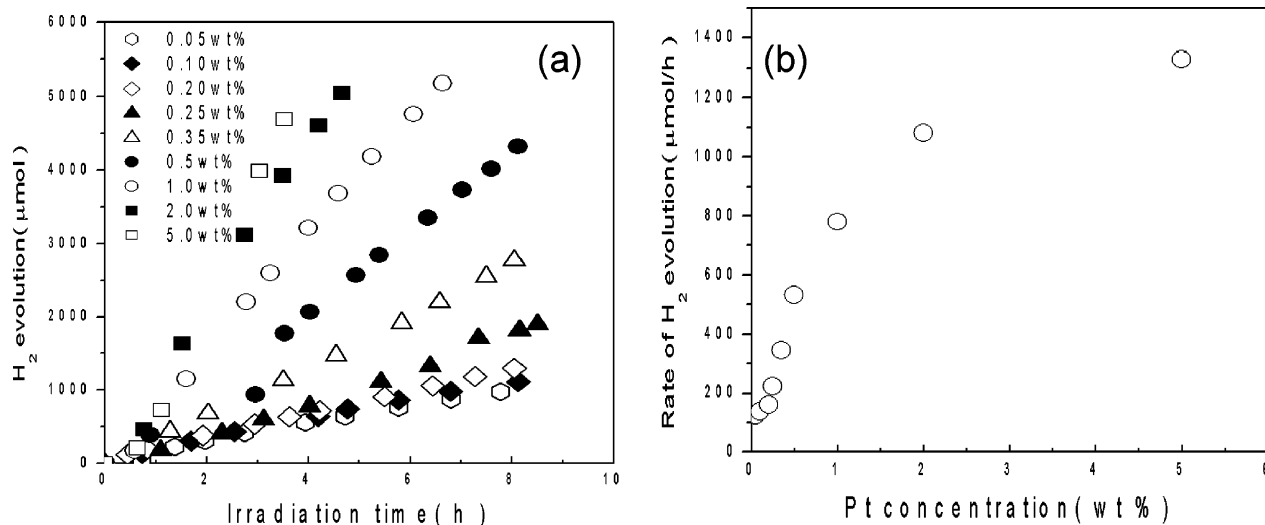


Figure 6. (a) Formation rates of the H_2 evolution from $\text{CH}_3\text{OH}/\text{H}_2\text{O}$ solution with Pt cocatalyst under UV light irradiation and (b) the Pt-loading dependence of the H_2 formation rates for the photocatalyst $\text{BaZn}_{1/3}\text{Nb}_{2/3}\text{O}_3$ (catalyst, 0.5 g; CH_3OH , 50 mL; H_2O , 320 mL; 400 W Hg lamp).

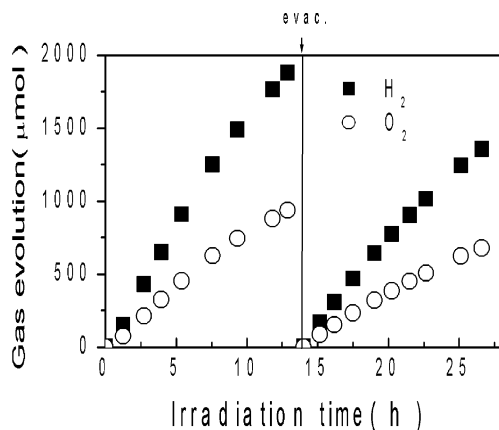


Figure 7. Formation rates of the H_2 and O_2 evolutions from pure water with the NiO_x cocatalyst under UV light irradiation for the photocatalyst $\text{BaZn}_{1/3}\text{Nb}_{2/3}\text{O}_3$ (catalyst, 0.5 g; co-catalyst, 1.0 wt %; H_2O , 370 mL; 400 W Hg lamp).

$\text{BaZn}_{1/3}\text{Nb}_{2/3}\text{O}_3$ is not mainly dominated by the cocatalyst concentration. The behavior in the Pt-loading dependence on the H_2 formation rate in $\text{CH}_3\text{OH}/\text{H}_2\text{O}$ solution is similar to that reported by Karakitsou et al. on TiO_2 .²⁸

Figure 7 shows the formation rates of H_2 and O_2 evolution from the NiO_x -loaded $\text{BaZn}_{1/3}\text{Nb}_{2/3}\text{O}_3$ particles suspended in pure water by using a magnetic stirrer under UV light irradiation (co-catalyst, 1.0 wt %, catalyst, 0.5 g; H_2O , 370 mL; 400 W Hg lamp). H_2 and O_2 evolution in a ratio of 2:1 was obtained at the same time. In the first run (about 13 h), the formation rates of H_2 and O_2 evolution are about 291.22 and 145.61 $\mu\text{mol}/(\text{h}\cdot\text{g catal})$, respectively. In the second run, the formation rates of the H_2 and O_2 evolutions changed a little, which may be ascribed to some physical loss, such as the adhesion on the surface of the plastic covered stirrer and the wall of the glass cell. In the case of the cocatalyst RuO_2 , the photocatalyst $\text{BaZn}_{1/3}\text{Nb}_{2/3}\text{O}_3$ also splits pure water into H_2 and O_2 in a chemical ratio of 2:1. The formation rates for H_2 and O_2 are about 97.2 and 48.6 $\mu\text{mol}/(\text{h}\cdot\text{g catal})$, respectively, much lower than those in the case of the cocatalyst NiO_x .

Film Characterization. To determine the flat-band potential of the photocatalyst $\text{BaZn}_{1/3}\text{Nb}_{2/3}\text{O}_3$, $\text{BaZn}_{1/3}\text{Nb}_{2/3}\text{O}_3$ (BZNO) film was deposited on a quartz substrate with an ITO bottom electrode by using a pulsed laser deposition (PLD) technique. Generally, ITO-glass substrates are employed as conductive substrates for photoanodes in photoelectrochemical reactions. However, because they cannot tolerate high temperature, ITO-covered quartz substrates were employed to accommodate the high crystallizing temperature of the $\text{BaZn}_{1/3}\text{Nb}_{2/3}\text{O}_3$ film. Figure 8 shows the X-ray diffraction pattern of the heterostructure BZNO/ITO/quartz as deposited by PLD at 850 °C. At 850 °C the films are well crystallized with pure phase. The transmittance spectrum of the heterostructure is shown in Figure 9. The heterostructure BZNO/ITO/quartz shows good optical transmittance. Here the wavelike form of the wavelength dependence of the transmittance should be ascribed to the different refractive indexes among the substrate, film and air.²⁹

Photoelectrochemical Characterization. Photoelectrolysis of water was performed in a Pyrex cell, which contained the photoanode, a Pt foil counterelectrode, a quartz window, and a saturated calomel electrode (SCE).

The model for the photoelectrolysis of water with semiconductor anodes has been well studied.^{30,31} The flat-band potential V_{FB} and the Fermi level E_{f} of the n-type semiconductor anode are important parameters. When a flat-band potential V_{FB} is applied on the semiconductor anode, the Fermi level of the

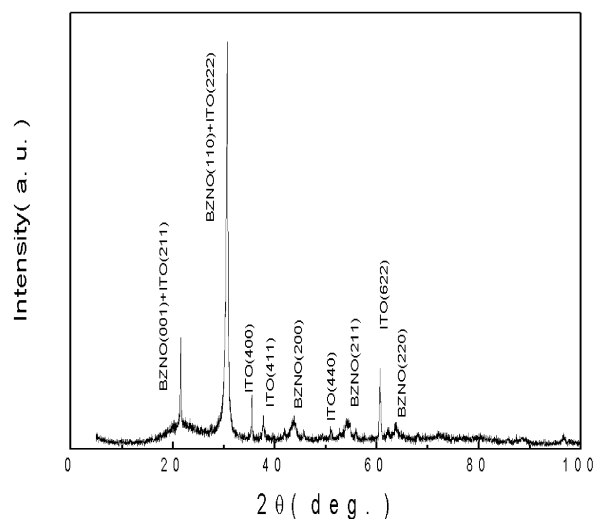


Figure 8. X-ray diffraction pattern of the heterostructure BZNO/ITO/quartz.

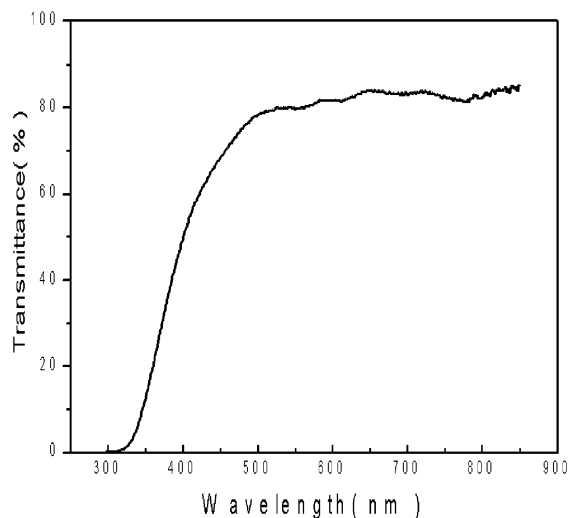


Figure 9. Wavelength dependence of the transmittance for the heterostructure BZNO/ITO/quartz.

semiconductor E_{f} is at the same line with the Fermi level of the conductive electrolyte E_{mf} . In this case no Schottky barrier exists at the interface between the semiconductor and the electrolyte. When $V - V_{\text{FB}} > 0$, the Fermi level of the semiconductor will be elevated higher than E_{mf} . Thus, the bands of the semiconductor near the interface bend upward. The internal electric field of the Schottky barrier formed at the interface separates the photoexcited electron-hole pairs and drives electrons into the interior of the semiconductor and then to the cathode through the external circuit, reducing water molecule. The holes move to the surface of the semiconductor, oxidizing water molecules. In this case, the photoelectrolysis of water appears. So, from the intersection point of the voltage-current curves in the case of the light turned on and turned off, we can roughly determine the flat-band potential V_{FB} .³²

Figure 10 shows the applied potential dependence of the photocurrent density for the heterostructure BZNO/ITO/quartz (500 W Xe lamp; electrolyte, 0.1 M Na_2SO_4 solution; pH = 5.92; scan rate (V/s), 0.1; electrode area, 0.44 cm^2). The dark current density at $V = 1.3$ V (vs SCE) is 1.65×10^{-6} A/ cm^2 , and the photocurrent density at $V = 1.3$ V (vs SCE) is 1.48×10^{-5} A/ cm^2 . The curve of the dark current density intersects with that of the photocurrent density at $V = -0.711$ V. It is known that the contact between ITO conductive electrode and

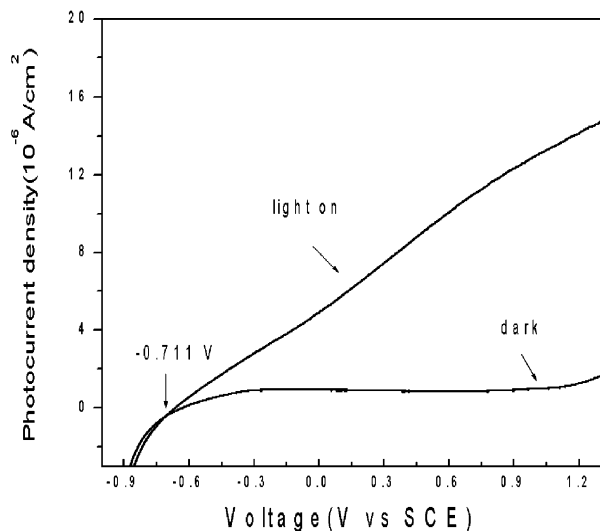


Figure 10. Applied potential dependence of the photocurrent density for the film photoanode $\text{BaZn}_{1/3}\text{Nb}_{2/3}\text{O}_3$ under the irradiation of a Xe lamp (500 W Xe lamp; electrolyte, 0.1 M Na_2SO_4 solution; pH = 5.92; scan rate (V/s), 0.1; electrode area, 0.44 cm^2).

the oxide semiconductor film is generally ohmic. From Figure 10, the flat-band potential of the semiconductor $\text{BaZn}_{1/3}\text{Nb}_{2/3}\text{O}_3$ can be roughly thought as -0.711 V vs SCE. Generally, due to surface ionization driven by adsorbed species, the flat-band potential shift of 0.059 V/pH unit is expected for the oxide semiconductor.^{33–35} So, the flat-band potential at pH = 0 is determined via extrapolation to be -0.362 V vs SCE (-0.121 V vs SHE). It was found that the potential at the bottom of most n-type oxide semiconductors is about 0.10 – 0.30 eV more negative than the Fermi level.^{36,37} Here, the film $\text{BaZn}_{1/3}\text{Nb}_{2/3}\text{O}_3$ was deposited at high partial pressure and annealed in pure O_2 atmosphere after the deposition (the density of oxygen vacancies is not so high), so the difference between the potential at the bottom of the conduction band and the Fermi level is approximately -0.30 eV . The potential at the bottom of the conduction band is then determined as -0.42 V (vs SHE). The potential at the bottom of the octahedrally coordinated oxide semiconductor $\text{Sr}_2\text{Nb}_2\text{O}_7$ has been approximately determined as about -0.90 V (vs SHE) by Kudo et al.³⁸ So, it is reasonably suggested that the lower conduction band determined for $\text{BaZn}_{1/3}\text{Nb}_{2/3}\text{O}_3$ should be the $\text{Zn}^{2+} 4s$ state. This conclusion is in agreement with the UV–vis diffuse reflectance spectrum of $\text{BaZn}_{1/3}\text{Nb}_{2/3}\text{O}_3$ as shown in Figure 5. The band gap (3.90 eV) determined from UV light absorption in the short wavelength region means that the potential at the bottom of the higher conduction band ($\text{Nb}^{5+} 4d$ state) should be around -0.90 V (vs SHE), because the potential at the top of the valence band ($\text{O} 2p$ state) is always around 3.0 eV below the standard hydrogen electrode (SHE) for perovskite oxides. Corresponding to the optical transition from the $\text{O}^{2-} 2p$ state to the $\text{Zn} 4s$ state, the band gap is determined about 3.42 eV ($\sim 363 \text{ nm}$). This is in accordance with its optical absorption as shown in Figure 5. The suggested band structure of $\text{BaZn}_{1/3}\text{Nb}_{2/3}\text{O}_3$ is plotted in Figure 5 as an inset.

Compared with the photocatalyst $\text{BaIn}_{1/2}\text{Nb}_{1/2}\text{O}_3$ with similar crystal structure,¹⁵ the photocatalytic activities of the photocatalyst $\text{BaZn}_{1/3}\text{Nb}_{2/3}\text{O}_3$ are about 3.1 times and 5.6 times the size of those of the photocatalyst $\text{BaIn}_{1/2}\text{Nb}_{1/2}\text{O}_3$ in the cases of $\text{CH}_3\text{OH}/\text{H}_2\text{O}$ and pure water under the same experimental conditions,¹⁵ respectively. Here the conduction band $\text{Zn}^{2+} 4s$ and the valence band $\text{O} 2p$ should play important roles in the photocatalytic activity of the photocatalyst $\text{BaZn}_{1/3}\text{Nb}_{2/3}\text{O}_3$.

IV. Conclusion

In summary, we have developed a new ABO_3 perovskite photocatalyst $\text{BaZn}_{1/3}\text{Nb}_{2/3}\text{O}_3$, in which the B site is occupied by two kinds of transition metals. The $\text{Zn}^{2+} 4s$ state acts as the lower conduction band instead of the $\text{Nb}^{5+} 4d$ state. Under UV light irradiation, the photocatalyst $\text{BaZn}_{1/3}\text{Nb}_{2/3}\text{O}_3$ shows favorable photocatalytic activity in splitting pure water into H_2 and O_2 . By increasing the surface area, modifying the surface conditions and reducing the band gap through N-doping, one can observe that the octahedrally coordinated photocatalyst containing transition metal ions with electronic configuration $ns^0(n-1)d^{10}$ should be one of the reasonable choices for water-splitting in the future.

References and Notes

- (1) Fujishima, A.; Honda, K. *Nature (London)* **1972**, *238*, 37.
- (2) Asahi, R.; Morikawa, T.; Ohwaki, T.; Aoki, K.; Taga, Y. *Science* **2001**, *293*, 269.
- (3) Zou, Z.; Ye, J.; Sayama, K.; Arakawa, H. *Nature (London)* **2001**, *414*, 625.
- (4) Yamaguti, K.; Sato, S. *J. Chem. Soc., Faraday Trans. 1* **1985**, *81*, 1237.
- (5) Sayama, K.; Arakawa, H. *J. Photochem. Photobiol. A* **1994**, *77*, 243.
- (6) Kudo, A.; Kato, H.; Nakagawa, S. *J. Phys. Chem. B* **2000**, *104*, 571.
- (7) Kudo, A.; Tanaka, A.; Domen, K.; Onishi, T. *J. Catal.* **1988**, *111*, 296.
- (8) Kato, H.; Asakura, K.; Kudo, A. *J. Am. Chem. Soc.* **2003**, *125*, 3082.
- (9) Hwang, D. W.; Lee, J. S.; Li, W.; Oh, S. H. *J. Phys. Chem. B* **2003**, *107*, 4963.
- (10) Kim, H. G.; Hwang, D. W.; Kim, J.; Kim, Y. G.; Lee, J. S. *Chem. Commun.* **1999**, 1077.
- (11) Kudo, A.; Sekizawa, M. *Chem. Commun.* **2000**, 1371.
- (12) Umebayashi, T.; Yamaki, T.; Itoh, H.; Asai, K. *J. Phys. Chem. Solids* **2002**, *63*, 1909.
- (13) Reber, J. F.; Meier, K. *J. Phys. Chem.* **1984**, *88*, 5903.
- (14) Sato, T.; Masaki, K.; Yoshioka, T.; Okuwaki, A. *J. Chem. Technol. Biot.* **1993**, *58*, 315.
- (15) Yin, J.; Zou, Z.; Ye, J. *J. Phys. Chem. B* **2003**, *107*, 61.
- (16) Yin, J.; Zou, Z.; Ye, J. *J. Phys. Chem. B* **2003**, *107*, 4936.
- (17) Sayama, K.; Yase, K.; Arakawa, H.; Asakura, K.; Tanaka, T.; Domen, K.; Onishi, T. *J. Photochem. Photobiol. A* **1998**, *114*, 125.
- (18) Domen, K.; Kondo, J. N.; Hara, M.; Tanaka, T. *Bull. Chem. Soc. Jpn.* **2000**, *73*, 1307.
- (19) Galasso, F.; Pyle, J. *J. Phys. Chem.* **1963**, *67*, 1561.
- (20) Fontana, M. D.; Metrat, G.; Servoin, J. L.; Gervais, F. *J. Phys. C: Solid-State Phys.* **1984**, *16*, 483.
- (21) Scalabrin, Chaves, A. S.; Shim, D. S.; Porto, S. P. S. *Phys. Status Solidi (b)* **1977**, *79*, 731.
- (22) Souza Filho, A. G.; Lima, K. C. V.; Ayala, A. P.; Guedes, I.; Freire, P. T. C.; Melo, F. E. A.; Mendes Filho, J.; Araujo, E. B.; Eiras, J. A. *Phys. Rev. B* **2002**, *66*, 132107.
- (23) Perry, C. H.; Khanna, B. N. *Phys. Rev.* **1964**, *135*, A408.
- (24) Galasso, F.; Darby, W. *J. Phys. Chem.* **1962**, *66*, 131.
- (25) Yin, J.; Zou, Z.; Ye, J. *J. Mater. Res.* **2002**, *17*, 2201.
- (26) Schroer, P.; Kruger, P.; Pollmann, J. *Phys. Rev. B* **1993**, *47*, 6971.
- (27) Zunger, A.; Freeman, A. *J. Phys. Rev. B* **1978**, *17*, 4850.
- (28) Karakitsou, K. E.; Verykios, X. E. *J. Catal.* **1992**, *134*, 629.
- (29) Yin, J.; Wu, Z. C.; Wang, Z. L.; Zhu, Y. Y.; Liu, Z. G. *J. Phys. D: Appl. Phys.* **1998**, *31*, 3185.
- (30) Wilson, R. H. *J. Appl. Phys.* **1977**, *48*, 4292.
- (31) Mavroides, J. G.; Kolesar, D. F. *J. Vac. Sci. Technol.* **1978**, *15*, 538.
- (32) Bard, A. J. *J. Phys. Chem.* **1982**, *86*, 172.
- (33) Butler, M. A.; Ginley, D. S. *J. Electrochem. Soc.* **1978**, *125*, 228.
- (34) Salvador, P. *J. Electrochem. Soc.* **1981**, *128*, 1895.
- (35) Chun, W. J.; Ishikawa, A.; Fujisawa, H.; Takata, T.; Kondo, J. N.; Hara, M.; Kawai, M.; Matsumoto, Y.; Domen, K. *J. Phys. Chem. B* **2003**, *107*, 1798.
- (36) Matsumoto, Y.; Omae, K.; Watanabe, I.; Sato, E. *J. Electrochem. Soc.* **1986**, *133*, 711.
- (37) Matsumoto, Y. *J. Solid State Chem.* **1996**, *126*, 227.
- (38) Kudo, A.; Kato, H.; Nakagawa, S. *J. Phys. Chem. B* **2000**, *104*, 571.